Journal of Metals, Materials and Minerals, 35(3), e2294, 2025

Photocatalytic performance of $Ba_{0.8}Ca_{0.2}TiO_3$ composite for norfloxacin removal in aqueous solutions

Raj MOHANTY[1], Swayam Aryam BEHERA[1], Asima SUBHADARSHINI[2], Binita NANDA[1], and P. Ganga Raju ACHARY[1,*]

[1] *Department of Chemistry, Faculty of Engineering and Technology (ITER), Siksha 'O' Anusandhan (Deemed to be) University, Bhubaneswar-751030, Odisha, India*

[2] *Environmental Science, Department of Chemistry, Faculty of Engineering and Technology (ITER), Siksha 'O' Anusandhan (Deemed to be) University, Bhubaneswar-751030, Odisha, India*

***Corresponding author e-mail**: pgrachary@soa.ac.in

Received date:
24 January 2025
Revised date:
22 April 2025
Accepted date:
9 June 2025

Keywords:
Norfloxacin;
Photodegradation;
Perovskite;
Environmental remediation;
Light absorption

Abstract

This study investigates the degradation of norfloxacin using a $Ba_{0.8}Ca_{0.2}TiO_3$ (BCTO) perovskite composite synthesized via a simple solid-state method. Variety of characterization techniques, including photoluminescence spectra, powder X-ray diffraction, UV-Vis diffuse reflectance spectra, FE-SEM and Fourier-transform infrared spectra confirm the structural and optical properties of BCTO. Electrical characterization further elucidates its conductive properties. The BCTO composite demonstrates an impressive 87% degradation rate of norfloxacin, attributed to its reduced electron-hole recombination, enhanced light absorption, and improved charge carrier mobility. Kinetic studies indicate that the degradation process adheres to a pseudo-first-order model, with BCTO outperforming both pure $BaTiO_3$ and conventional photocatalysts. These findings highlight the potential of BCTO as an effective material for environmental remediation, specifically for degrading persistent pharmaceutical contaminants like norfloxacin.

1. Introduction

One of the most important classes of fluoroquinolone which has been more than often used in the field of antibiotics for controlling bacterial infections is Norfloxacin (NOR) [1,2]. Just like numerous other antibiotics, NOR is not well metabolised by humans or other animals, and when over 75% of it is released into aquatic environments, it ends up everywhere just like in wastewater curation facilities, in pharmaceutical wastewater, and in surface water bodies and eventually contributes to the development of antimicrobial resistance that poses a great threat to human health and the ecosystem as a whole. Therefore, numerous approaches for removing antibiotics from aquatic ecosystems have been investigated till date [3-8]. Among them, photocatalysis, which converts solar energy into active species and enables the break-down of antibiotics into smaller, less hazardous molecules, has drawn a lot of interest [9]. Whenever a semiconductor photocatalyst is exposed to light, its conduction band and valence band, respectively, produce electrons (e^-) and holes (h^+), which are both involved in the redox processes that lead to photodegradation. However, most semiconducting materials suffers from photogenerated charge recombination, which restricts the catalytic efficiency of the photo-REDOX processes for useful purposes [10].

The techniques applied by various environmental engineers to remove NOR from contaminated water systems using typical adsorption techniques are getting a lot of attention. Prior studies have shown that advanced oxidation processes (AOPs) might be utilised to absorb, degrade and remove NOR. Popular AOPs, such as photocatalysis, ozonisation, UV, electro-fenton, $KMnO_4$, UV/O_3, UV/TiO_2 and UV/H_2O_2 have efficiently eliminated NOR [11,12]. AOPs are thus regarded as successful strategies for the breakdown and extraction of organic molecules from any effluent, including medicines, due to the production of hydroxyl radicals. However, AOPs have limitations, such as being unable to eliminate later stage regenerative chemicals. A heterogeneous composite-mediated visible light photocatalysis is widely accepted as a solar light-mediated technology due to its outstanding performance and energy efficiency [13].

One of the most widely used photocatalysts in environmental applications is Barium Titanate ($BaTiO_3$), a semiconductor with good dielectric/ferroelectric properties [14] and perovskite structures due to its low cost, chemical stability, and non-toxicity [15,16]. Because of a variety of advantageous characteristics, such as suitable band positions, massive oxygen vacant positions, numerous crystalline structures, the capability for band bending, rapid movement of photogenerated charge carriers, spontaneous polarisation, and size and shape customisation, different kinds and forms of $BaTiO_3$ have demonstrated higher efficacy towards the overall photocatalytic processes. However, $BaTiO_3$'s overall photocatalytic impact is restricted by its wide band gap and recombination of electron/hole pairs. It is possible to expand light harvestation property of $BaTiO_3$ into the visible spectrum by altering its opto-electronic properties, which would solve these issues.

To solve this problem of large band gap we incorporate various materials into the perovskite to make it more likely to be show great photocatalytic properties. Among many elements, Calcium (Ca) showed the best results. After incorporation of calcium into the $BaTiO_3$ crystal, the bandgap shows that near the G-point, the band positions has shifted from indirect to direct band positions [17,18]. The band structure changes once Ca is incorporated into the perovskite, causing the conduction band (CB) to move towards a higher energy level. Studies on electronic aspects have been undertaken to investigate how various orbitals contribute to the VB and the CB positions. The reports were examined for modification in various optical properties like absorption, reflectivity, refractive index, extinction coefficient, conductivity, dielectric function and loss function between the energy range from 0 eV to 30 eV. The UV light area has the most prominent optical energy and absorption peak. The theoretical investigation indicates that the modified $BaTiO_3$ solution is an excellent match for the photorefractive and optoelectronic devices based on the material's optical properties. The presence of the covalent link and mechanical stability of certain compounds can be determined by various elastic constants. As a result, introduction of Ca atom into the $BaTiO_3$ perovskite greatly developed a number of extraordinary features that led to its multifunctional uses [19].

Calcium incorporation in barium titanate ($BaTiO_3$) significantly modifies its structural, electronic, and dielectric properties [20]. Ca ions primarily substitute Ba at the A-site, inducing lattice distortion and oxygen vacancies that enhance optical absorption and electrical permittivity. However, excessive Ca infusion reduces the tetragonal phase fraction and can form secondary calcium titanate phases, which degrade ferroelectric performance and dielectric constant [21]. Ca infusion with barium mitigates these negative effects by stabilizing the tetragonal structure, suppressing secondary phases, and improving grain growth and densification. These structural changes lead to enhanced piezoelectric and dielectric properties, making Ca infused $BaTiO_3$ a promising lead-free ceramic for energy storage and electronic applications [22].

2. Experimental method

2.1 Synthesis method

A simple solid state reaction method was employed for the preparation of the composite. A stoichiometric ratio of $BaCO_3$ (Sigma-Aldrich, 99%) along with $CaCO_3$ (Merck, 99%) and TiO_2 (Alfa Aesar, 99.9% purity) were ground together in a mortar pestle for three hours and methanol being added to it continuously to prepare the required composition of $Ba_{0.8}Ca_{0.2}TiO_3$ composite. The mixture was calcined in the muffle furnace at a temperature of 1050°C with heating rate of 5°C.min^{-1} after three hours of continuous grinding. Subsequently, the pure BCTO composite was formed. The formation of the obtained composite was then verified by different characterisation methods.

2.2 Characterisation

The composite's X-ray diffraction (XRD) spectra were obtained using Rigaku Mini flex diffractometer with a 10° to 90° scanning range (at λ = 1.5406 Å CuKα radiation). Using Jasco-750 UV-Vis Spectrophotometer and boric Acid as a reference, the samples were exposed to UV-visible diffuse reflectance spectroscopy (UV-DRS) within the range of 200 nm to 800 nm range. The vibrational modes of all the catalysts were measured using the Jasco FT/IR-4600LE in order to determine the functional group present using the Fourier transform infrared spectrograph (FTIR). The Hitachi F-4600 was used to analyse the Photoluminescence spectra under ambient temperature settings. For the electrical parameters, a LCR meter N4L (PSM 1735, computer controlled) was used.

2.3 Photocatalysis

Using the synthesised catalyst BCTO, application of photocatalysis to combat the antibiotic medication and norfloxacin's degradation was studied under solar radiation. The photocatalyst was immersed in 20 mL of drug solution 40 ppm and stirred for 30 min in the dark in order to preserve the adsorption-desorption equilibrium. In Bhubaneswar, Odisha, the drug solution was exposed to sunlight for a period of 75 min at an intensity of 100,000 lux to observe how it degraded. Afterwards, by the process of filtration the catalyst was separated out from the drug solution after degradation, the filtrate was analysed at 275 nm using a UV-visible spectrophotometer. The photooxidation of the photocatalyst on Norfloxacin was determined using the formula given below:

$$\text{Efficiency } (\%) = \frac{C_i - C_t}{C_i} \times 100 \quad (1)$$

Where C_i is the initial drug concentration
C_t is the final drug concentration

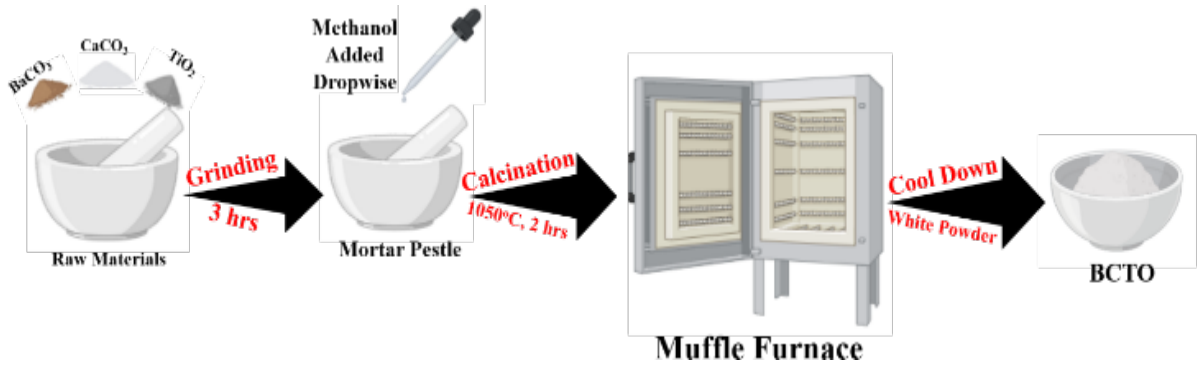

Figure 1. Synthesis method of BCTO.

3. Result and discussion

3.1 X-ray diffraction (XRD)

The X-ray diffraction (XRD) reflection of the $Ba_{0.8}Ca_{0.2}TiO_3$ is shown in the Figure 2(a) which was acquired by using CuKα monochromatic radiation ($10° \leq 2\theta \leq 90°$) using a Rigaku X-ray diffractometer. The XRD patterns were matched with JCPDS no 01-075-0460 which reveals the formation of a tetragonal phase with lattice parameter a=3.993, b=3.993, and c=4.034 (α= β = γ =90°) [23,24]. Among the various peaks that was found the strong prominent peak (101) is found to be at 2θ=31.49° and other phases at 2θ=22.23° (100), 31.49° (101), 33.14° (110), 38.89° (111), 45.37° (200), 47.6° (002), 56.27° (211), 65.75° (202), 75.07° (301), 79.44° (311) and 83.50° (222) confirmed the formation of the perovskite $Ba_{0.8}Ca_{0.2}TiO_3$. The other minor diffraction peaks in the XRD pattern correspond to the $CaCO_3$ phase due CO_2-rich atmosphere during cooling which can lead to partial retention or reformation of $CaCO_3$ on the sample surface.

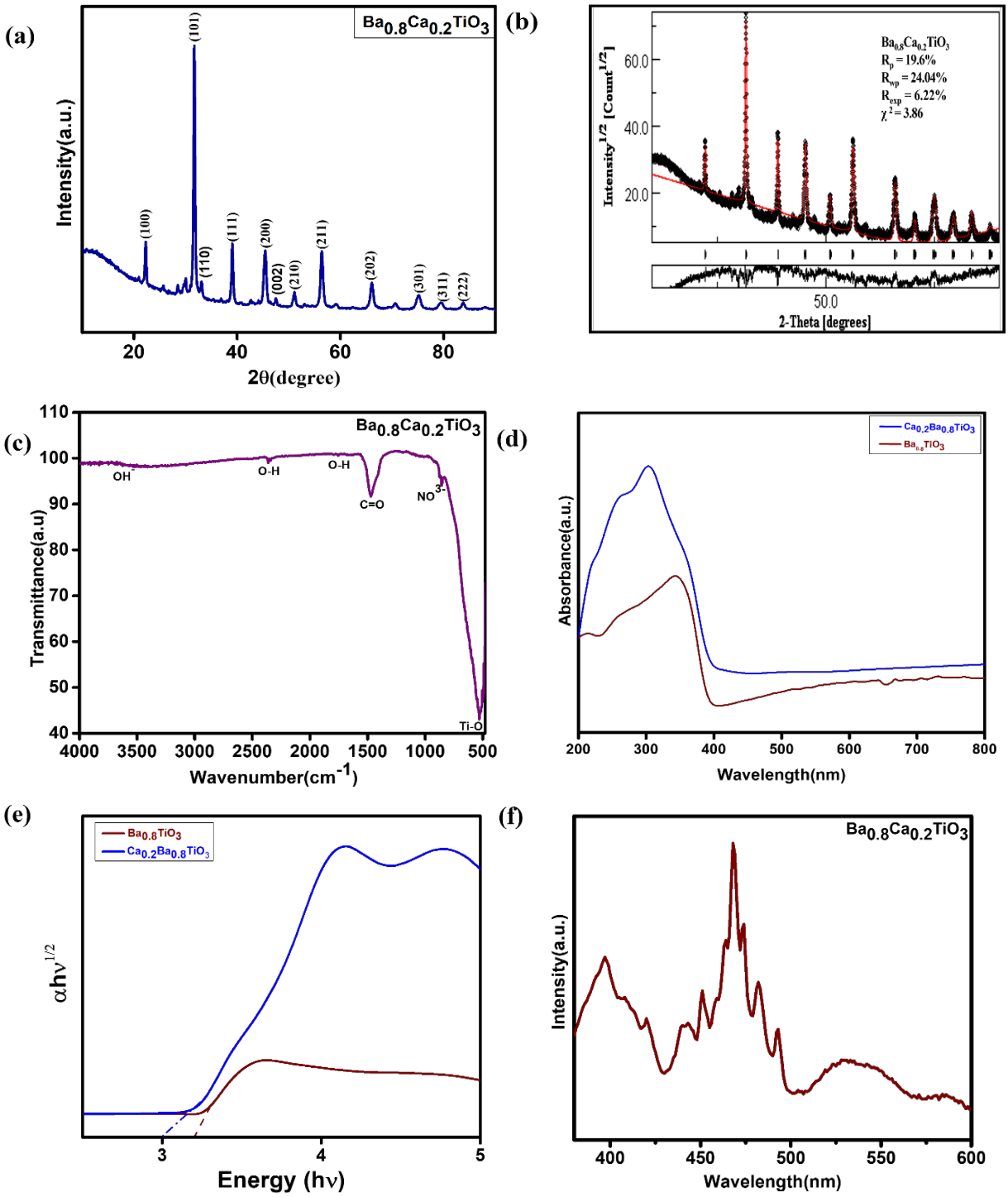

Figure 2. (a) XRD reflection of $Ba_{0.8}Ca_{0.2}TiO_3$, (b) Rietveld refinement analysis of XRD pattern of $Ba_{0.8}Ca_{0.2}TiO_3$, (c) FTIR spectra of $Ba_{0.8}Ca_{0.2}TiO_3$, (d) UV-VIS-DRS absorbance spectra, (e) Direct energy band gap of $Ba_{0.8}Ca_{0.2}TiO_3$, and (f) Photoluminescence (PL) spectra of the $Ba_{0.8}Ca_{0.2}TiO_3$.

Table 1. X-ray diffraction positions (2θ) and the interplanar spacing values d-spacing (Δd).

2 Theta	Relative intensity	d-spacing (Δd)
22.241	16.2	0.0159
31.495	100	0.01729
38.896	24.6	0.00818
45.379	35.3	0.00245
51.096	7.1	0.00017
56.282	35.1	0.00232
65.748	19.7	0.00474
70.345	4	0.00373
75.166	13.7	0.00022
79.449	6.4	0.0011
83.502	5.4	0.00239
88.118	1.5	0.00169

The Rietveld refinement of BCTO powders at room temperature is shown in Figure 2(b). With R_p value at 19.6%, R_{wp} value at 24.04%, R_{exp} value of 6.22% and with a sigma value (χ^2) of 3.86, which are good fitting parameters, indicate that the resulting samples are of high quality. It is possible to correctly correlate each peak with the perovskite structure. The X-ray diffraction peak positions (2θ) and corresponding interplanar spacing values (d-spacing, Δd) have been calculated and are presented in Table 1, with all Δd deviations remaining below 0.05 Å.

3.2 Fourier transform infrared spectroscopy (FTIR)

The FTIR spectra of $Ba_{0.8}Ca_{0.2}TiO_3$ is displayed in the Figure 2(b). A noticeable absorption peak that corresponds to the vibrational frequency emerges at around 530 cm^{-1}. This adsorption peak corresponds to both symmetric and asymmetric stretching of the Ti-O (TiO_6) octahedron bonds and emphasises their deformation. This band showed a broadening and a little shift to a higher wavenumber, indicating that the stretching of the Ti-O link of $BaTiO_3$ was the source of the equivalent mode of $Ba_{0.8}Ca_{0.2}TiO_3$. Since the cation Ca^{2+} has a lower electric charge than Ti^{4+}, the weak coulomb interaction is the cause of this. The M-O (cation-oxygen) bond has less energy because Ca^{2+} and O_2^- have a lower electrostatic Coulomb interaction than Ti^{4+} and O_2^-. The shift may also result from the substitution of Ca^{2+} for Ba^{2+}, which reduces the material's cell volume as Ca^{2+}'s ionic radii (1.34 Å) are smaller than that of Ba^{2+}'s (1.61 Å). The wavenumber of absorption increases when the direct cell volume decreases and the electrostatic coulomb force interaction increases as a result of the order-disorder shrinking of the Ti-O octahedral distance. The most significant bands that correspond to the ionic NO_3^- (853 cm^{-1}) introduced to the solution by barium, calcium and titanium catalyst are additionally identified as $Ba(NO_3)_2$, $Ca(NO_3)_2$ and $TiO(NO_3)_2$ in the case of the modified precursors. The presence of carbonates is shown by the well-defined absorption band at around 1473 cm^{-1} in the $Ba_{0.8}Ca_{0.2}TiO_3$ material. This band can be represented by the C=O vibration. The presence of O-H bonds is indicated by sharp bands in the sample's FT-IR spectra around 1752 cm^{-1} and 2359 cm^{-1}. According to the OH- groups, the band is visible at around 3525 cm^{-1}. These additionally demonstrates the defects caused by OH– groups in the titanium lattice formation, which are frequent in hydrogen bonding systems. The prominent absorption band at around 1473 cm^{-1}, which is well-defined in materials containing Ca^{2+} ions and is corroborated by results of the XRD test which indicates the presence of carbonate peaks [25,28].

3.3 Ultraviolet-visible diffuse reflectance spectroscopy (UV-DRS)

UV-Vis DRS spectra were used to examine each crystal's optical properties. The absorbance spectra of the pristine $Ba_{0.8}TiO_3$ as well as that of the BCTO ($Ba_{0.8}Ca_{0.2}TiO_3$) is shown in Figure 2(c). The BCTO's broad absorbance spectrum between 200 nm and 400 nm is seen. This suggests that all catalysts have visible spectrum reactions and display the traits of a semiconducting photocatalyst that is active to visible light. The following formula was used to obtain the band gap of the pristine $Ba_{0.8}TiO_3$ along with the BCTO sample using UV-visible DRS spectroscopy [7,29].

$$\alpha h\nu = A\left(h\nu - E_g\right)^n \quad (2)$$

Where, A is the proportionality constant, υ is the frequency of light, E_g is the bandgap energy, and the "n" is an exponent that represents the nature of band transition (the indirect allowed and forbidden transitions are represented by n=1/2 and n=3/2). The optical band gap of the $Ba_{0.8}Ca_{0.2}TiO_3$ was calculated by extending the figure on the energy axis to the energy axis intercept ($\alpha h\upsilon^{1/2}$ vs $h\upsilon$) as shown in Figure 2(d) found as 3.0 eV and the band gap for $Ba_{0.8}TiO_3$ was found to be 3.2 eV. However, addition of calcium improves visible light absorption, which boosts photocatalytic activity of Norfloxacin.

3.4 Photoluminescence (PL)

Photoluminescence (PL) spectroscopy is one of the most important techniques for analysing energy levels inside the band gap to ascertain the extent of structural anomalies in the material. The phenomenon that is brought on by incident photons is referred to as 'photoluminescence'. It is commonly caused by self-trapped excitons, polarised states, and oxygen vacancies in perovskites. The separation of photogenerated charge carriers from their excited state was investigated using the PL spectra of produced $Ba_{0.8}Ca_{0.2}TiO_3$ nanoparticles. PL spectra was obtained when the nanoparticles were stimulated at 350 nm at room temperature. In this case, as shown in Figure 2(e) it was discovered that the emission maxima for $Ba_{0.8}Ca_{0.2}TiO_3$ nanoparticles is in the range of 397 nm to 467 nm.

3.5 Electrical

A higher dielectric constant indicates that the material functions as a capacitor by retaining more electrical charge. In order to efficiently accumulate and use produced charges during the photocatalytic process, this might prove advantageous. The dielectric constant affects how strong the electric field is inside the material, which affects how the drug molecule and catalyst interact [30,31]. Charge transfer and drug adsorption can both be improved by a stronger field. Figure 3(a) represents the plot of dielectric constant (ε′) vs frequency for the BCTO. The dielectric constant falls as the frequency rises, as the graph indicates. This is the most typical behaviour observed in a range of materials, and it may be attributed to how the charged carriers react to the applied electric field [32]. At higher frequencies, the reaction time of the charge carriers to the alternating electric field is shortened, which results in a lower electric constant.

The impedance analysis of BCTO sample reveals information on its electrical properties. Considering different aspects, including grain, interfaces and grain borders, to a material's electrical behaviour may be achieved through the use of impedance analysis. The real part (Z′) and the imaginary part (Z″) make up the complex impedance (Z*). The actual component is represented by resistance (R), whereas the imaginary part is represented by capacitance (C). It is accompanied by the relaxation time (T), which is determined by multiplying the resistance by the capacitance (τ=RC), and the angular frequency (ω) [33,34]. The capacitance (C) represents the imaginary part whereas resistance (R)represents the real part. Along with it the angular frequency (ω) and the relaxation time (τ), which is given by the product of resistance and capacitance (τ=RC).

$$Z^* = Z' + jZ'' \text{ and } Z'^2 + Z''^2 \quad (3)$$

$$Z' = \frac{R}{1+(\omega\tau)^2} \text{ and } Z'' = \frac{\omega R}{1+(\omega\tau)^2} \quad (4)$$

The curve of Z′ against frequency for the reported $Ba_{0.8}Ca_{0.2}TiO_3$ is shown in Figure 3(b). The findings demonstrate that when temperature and frequency rise, Z′ value drops. Low frequency dispersion is seen at various temperatures, demonstrating a frequency dependent behaviour. Furthermore, value of Z′ which is independent of frequency arises at high frequencies at all temperatures. The presence of low frequency dispersion in Z′ suggests the presence of vacancies or flaws in the material, but the frequency independent behaviour at high frequencies reveals that there is no space charge polarisation at the grain boundaries brought on by the ion inertia. Figure 3(c) focuses on the imaginary part of the impedance, Z″ with frequency for the BCTO sample. It is observed that initially up to the frequency range of 10,000 Hz the Z″ value increases but after that its value gradually starts dropping. There can be several reasons for this dielectric behaviour of the composite above 10,000 Hz [35]. The known reasons for this unusual behaviour of the sample may be dielectric resonance phenomena, relaxation, breakdown events, interfacial impacts, impurities or defects and measurement distortions.

The BCTO shows electrical conductivity which was calculated by the following Equation:

$$\sigma_{ac} = \omega\varepsilon_o\varepsilon_r tan\delta \quad (5)$$

where, ω is the dielectric permittivity of the BCTO material and is computed as 2π times the frequency f, while ε_o is the dielectric permittivity of vacuum. Figure 3(d), a plot of electrical conductivity is displayed, which demonstrates a clear frequency dependence and spans the frequency from 1 KHz to 1 MHz. With increasing frequency, the AC conductivity (σ_{AC}) values show a constant growth pattern. The power law equation is consistent with this behaviour which is given by the following Equation:

$$\sigma(\omega) = \sigma_o + \omega^n \quad (6)$$

where, the frequency exponent (n) typically falls within the range of 0.6 to 1. Better frequencies correspond to better conductivity, a tendency that is consistently backed by the underlying hopping process. The interaction between the current charge carriers collectively determines the conductivity behaviour of the material. Within the framework of this research, the integration of the Calcium in the $BaTiO_3$ composite leads to decreased charge formation, therefore reducing the inter-charge hopping distance. This characteristic can be attributed to the boosted charge transfer and the amplified density of conductive channels inside the composites. At lower frequencies, the ac conductivity is minimum but as the frequency range increases the ac conductivity increases.

The change of frequency against tangent loss is given in Figure 3(e). The graph demonstrates that the misalignment of the electric dipoles is the reason of the large dispersion of dielectric loss (tan δ) at less frequency zone. The Maxwell-Wagner polarisation effect can explain this sort of dispersion properties of both the dielectric loss and dielectric constant at low frequency zone. According to this hypothesis, the dielectric medium is firmly supported by resistive grain boundaries that are sensitive to low frequency and conducting grains that are sensitive to high frequency. Mobile ions between Ti^{3+} and Ti^{4+} hop at their respective octahedral positions at low frequencies, however, at high frequencies this hoping process is reduced because of the rapid changes on the external AC field that are provided. Because of this hoping mechanism, electrons can pass across weak conducting grain boundaries and conducting grains.

The resulting Nyquist plot Figure 3(f) typically displays a semi-circular curve, which reflects the dielectric relaxation behaviour of the material. In the equivalent circuit model used for data fitting, 'C', 'Q', and 'R' represent different electrical components: 'C' corresponds to the bulk capacitance (C_b), 'Q' is a constant phase element (CPE) accounting for non-ideal capacitive behaviour, and 'R' represents the bulk resistance (R_b). By fitting the experimental data to the (CQR) (CR) equivalent circuit, the intrinsic electrical characteristics of the material, such as C_b, Q, and R_b, are extracted [8,29]. Additionally, this model enables the evaluation of grain-boundary properties, including grain-boundary resistance (R_{gb}) and grain-boundary capacitance (C_{gb}), which are essential for understanding the interfacial effects within the material. The semicircular nature of the plot is primarily attributed to the bulk contribution, while deviations or additional arcs at lower frequencies typically signify grain-boundary effects. Table 2. displays the circuit parameter data of BCTO measured at room temperature.

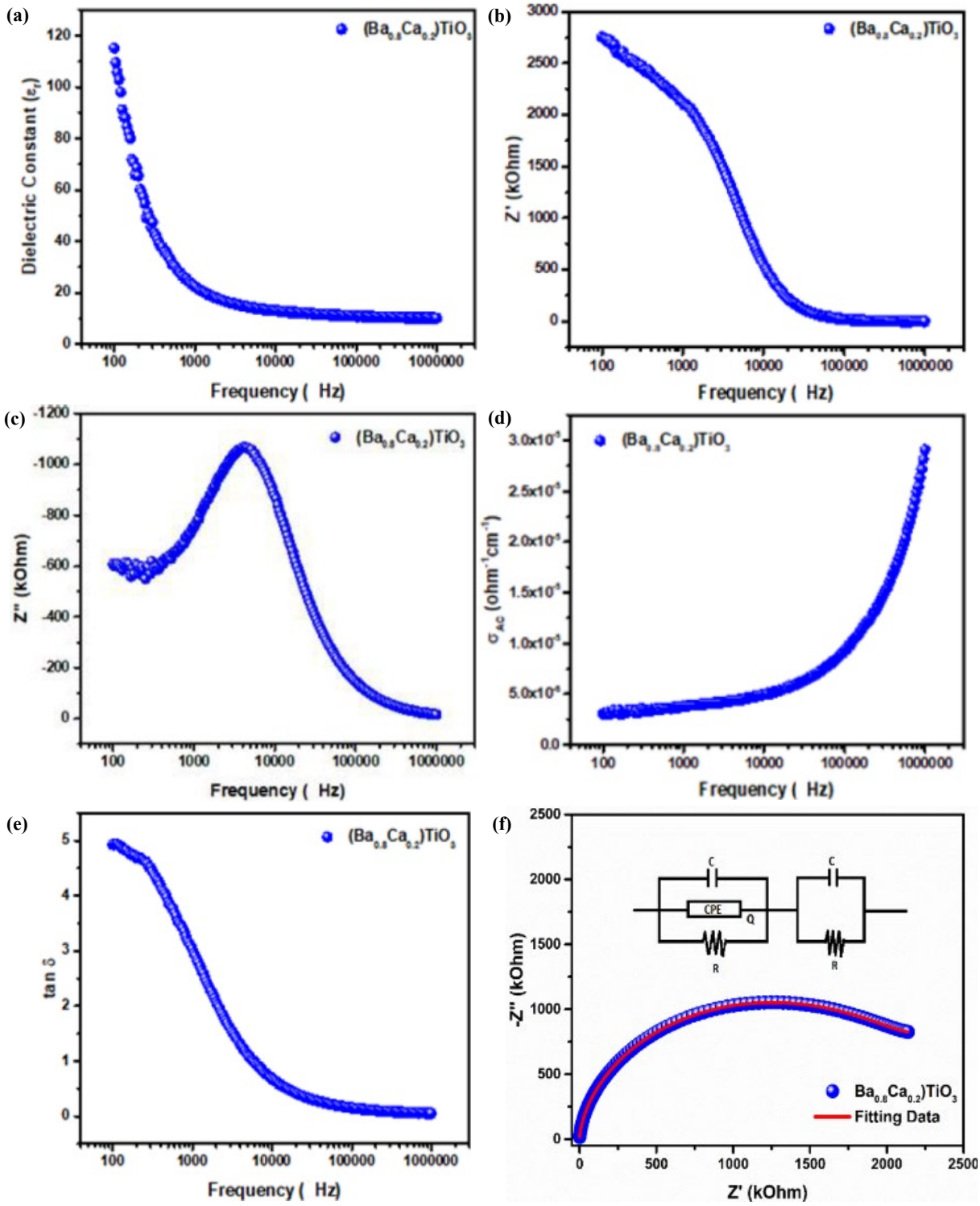

Figure 3. (a) Frequency dependent dielectric constant, (b-c) Frequency dependent real and imaginary impedance, (d) Frequency dependent electrical conductivity, (e) Frequency dependent tangent loss, and (f) Nyquist plot with circuit fitting.

Table 2. Circuit parameter data of BCTO at room temperature.

C_b [nF·cm^{-2}]	Q [S.sec^5·cm^{-2}]	n	R_b [ohm·cm^{-2}]	C_{gb} [F·cm^{-2}]	R_{gb} [ohm·cm^{-2}]
9.32×10^{-12}	2.53×10^{-10}	6.32×10^{-1}	2.47×10^{6}	5.67×10^{-10}	1.10×10^{16}

3.6 Field emission scanning electron microscope (FE-SEM)

Significant differences in the structural morphology and elemental composition can be observed in the FE-SEM images of BCTO before and after photocatalytic degradation with NOR solution, thus, emphasising the effects of photocatalytic treatment. The BCTO display a reasonably homogeneous and smooth surface with distinct, linked nanoparticle frameworks before undergoing photocatalysis as shown in Figure 4(a). There is no indication of any foreign elements as per the Energy dispersive spectroscopy (EDS) analysis which confirms the existence of basic elements which include Barium (Ba), Calcium (Ca), Titanium (Ti) and Oxygen (O) as represented in Figure 4(c). Whereas, after photocatalysis the BCTO display a substantially altered surface morphology which includes increased surface roughness and more agglomeration on the surface, which is an indication of the NOR solution's photocatalytic degradation. This modification implies removal of organic materials from the composite surface during the photocatalytic process as depicted in Figure 4(b). The EDS analysis shows a change in elemental composition of the composite after photocatalysis which indicates the breaking down of organic contaminants during photocatalytic process as shown in Figure 4(d). The elemental mapping also confirms the presence of important organic components such as Oxygen (yellow), Nitrogen (red), Carbon (sky), Calcium (green), Barium (pink) and Titanium (blue) as represented in Figure 4(e-f) which confirms the photocatalytic degradation of NOR. Presence of organic elements like Nitrogen and Carbon supports the fact that degradation of NOR has taken place successfully [32]. This comprehensive study demonstrates that the photocatalytic process substantially alters the surface morphology as well as the elemental composition hence, enhancing their photocatalytic performance for environmental applications.

3.7 Photocatalytic degradation of norfloxacin (NOR)

Ca incorporated $BaTiO_3$ was utilised to determine the photocatalytic breakdown efficiency of the antibiotic drug Norfloxacin (NOR) in the presence of visible light. A batch mode reaction technique containing 40 ppm of NOR and an optical dosage of 0.6 mgL^{-1} at a basic pH of 8. The reaction initially took place in a dark place for 30 min, and then it was kept in solar light illumination for 75 min, as indicated in the figure, in order to maintain the adsorption-desorption equilibrium. As a result, the norfloxacin photocatalytic reaction was optimised for a time period of 75 min. Pollutant adsorption on the catalyst surface is a key factor in photocatalytic reactions. Adsorption is mostly dependent on the positive and negative charges that are created on the surface by keeping the substrate's pH stable.

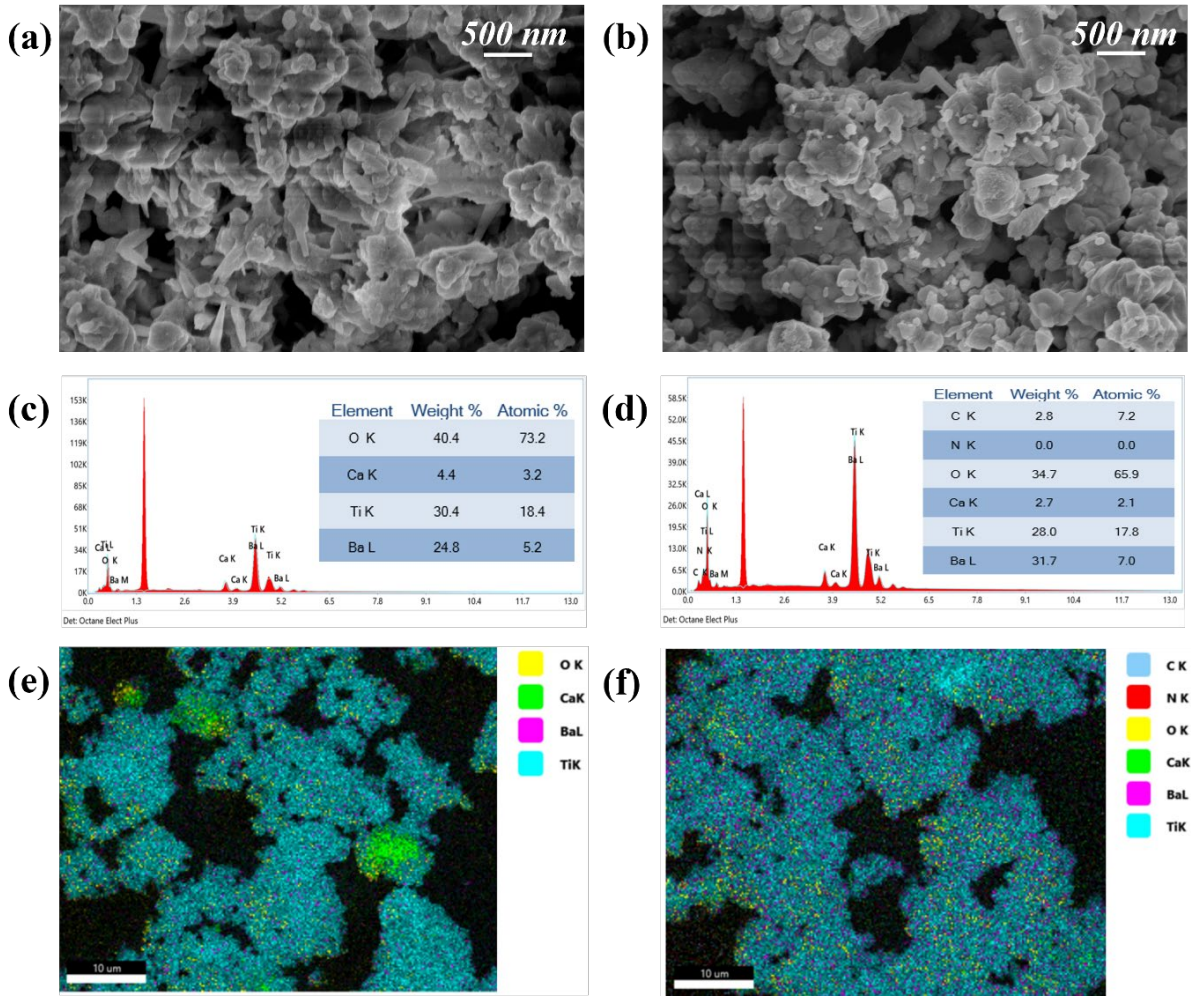

Figure 4. (a, b) FE-SEM images of BCTO before and after photocatalysis, (c, d) EDS analysis of BCTO before and after photocatalysis, (e, f) Elemental mapping of BCTO before and after photocatalysis.

3.7.1 Adsorption-desorption

The photo-oxidation rate of the BCTO composite for NOR was calculated using unmodified $BaTiO_3$ as a reference catalyst. It was found that the modified composite showed better photo-oxidative properties than the pristine. From 15 min to 75 min, the rate of absorption showed a steady decrease with time, attaining the adsorption-desorption equilibrium after 75 min. The greatest absorption peak is seen at 275 nm, as shown in Figure 5(a) The peak intensity gradually decreased with time. The lowest rate of absorption was marked at 75 min. Since, adsorption rate and rate of photocatalytic degradation are closely linked, 75 min was determined to be the ideal duration for further photocatalysis.

3.7.2 Effect of pH

The influence of pH is a crucial factor for the oxidation of antibiotic due of its chemical components. The two photon rings i.e., fluoroquinolines and the piperazinyl side chain that occur in diverse combinations and have varying Pk_a NOR values. This may be represented as follows:

$$NOR^{2+}(Dicationic) \underset{5.10}{\overset{Pk_a1}{\rightleftharpoons}} NOR^{+}(Monocationic) \underset{5.85}{\overset{Pk_a2}{\rightleftharpoons}} NOR^{\pm}(Zwitterionic) \underset{8.10}{\overset{Pk_a3}{\rightleftharpoons}} NOR^{-}(Anionic)$$

Within a certain pH range, the photo-reactivities of the ionic species would determine the rate of photo-oxidation. Here, the experiment was conducted over a variety of pH values (3, 5, 8, 10). The most important factor that determines the surface charge is point zero charge (pH_{pzc}). The pHpzc value determines at what value of pH the catalyst surface achieves electrical neutrality. The catalyst surface is positively charged if the pH is less than the pHpzc value and negatively charged if the pHpzc value is greater. As the NOR and the catalyst are positively charged in the acidic medium, electrostatic repulsion takes place, preventing the NOR from absorbing on the catalyst surface and lowering the photo-oxidation efficiency. It functions as a zwitterion and has positive and negative charge in the pH range of 5 to 7, which is near to the first Pk_a of NOR. This arrangement facilitates the photooxidation process by promoting attraction between the negatively charged NOR and the positively charged catalyst surface. The observation matches up with Figure 5(b) Using BCTO as a reference catalyst, this illustrates the impact of the NOR solution's starting pH value. The degradation plot seems an inclination with the increase in pH with its highest at 8 and then decreases.

3.7.3 Effect of Concentration of NOR

Upon analysis we got to know how the concentration of NOR affected the photocatalytic process. The kinetic research illustrates how NOR affects photo-oxidation at various dosages (20 mgL^{-1}, 40 mgL^{-1} and 60 mgL^{-1}) at various time periods ranging between 15 min to 75 min. The pseudo first order reaction kinetics were followed which is depicted in Figure 5(d). The observed data matched successfully to the pseudo-1st order kinetics as shown in equations C_i.

$$K_{app}t \times 2.303 = \log\frac{C_i}{C_t} \quad (7)$$

$$K_{app} = \log\frac{C_i}{C_t} \times \frac{2.303}{t} \quad (8)$$

The relation between C_i and C_t is defined as C_i/C_t as a function of degradation time. K_{app} is the symbol for the observed rate constant. As per the efficiency of photo-oxidation, BCTO holds the largest rate constant for photo-oxidation (K_{app}), and the coefficient of co-relation is almost equal to 1, demonstrating that the kinetic model can accurately depict NOR's degradation. The graph between rate of reaction and time shows that the photo-oxidation efficiency decreases as the NOR concentration rises. This could be because of the increased NOR concentration prevents the catalyst from using light, or it could be because more NOR molecules adhere to the catalyst's active site, affecting its ability to absorb sunlight. For this reason, 40 ppm (40 mgL^{-1}) was kept same for subsequent observations.

3.7.4 Effect of dosage of catalyst

A catalyst dose-dependent experiment involving the catalyst BCTO was caried out at pH 8 for 40 ppm. The vast number of active sites allowed NOR to achieve a maximum removal efficiency of 87% in 0.06 g. Because it may block light radiation and hinder NOR's capacity to photo-oxidise, as seen in Figure 5(c), the catalyst solution interaction first increased and then decreased as the dosage rose.

3.7.5 Reusability or stability test

The photostability of the synthesized BCTO sample was investigated by recycling photo-oxidation employing NOR under visible light irradiation. The experimental settings and parameters were unchanged i.e, pH 8 with 0.06 g of sample for 75 min. After four rounds it was found that there was no change in degradation percentage as demonstrated in Figure 5(g).

3.7.6 Role of scavengers

A scavenging experiment was conducted in order to identify the primary reactive oxidative species involved in the photo-oxidation of NOR. Various scavengers (1 mM) such as citric acid (CA), parabenzoquinone (PBQ), isopropanol (IP) and dimethyl sulfoxide (DMSO) are utilised to quench e^-, $^{\bullet}OH$, O_2^-, h^+ respectively. The degradation of NOR was not significantly impacted by the addition of IP, as seen in Figure 5(f). This indicates that the OH radical plays a minor role in the photo-oxidation process. On the other hand, the photo-oxidation of NOR was inhibited by the presence of CA and PBQ. The finding indicates that the main active species in the process of photo-oxidation brought on by the BCTO system are O_2^-, h^+. Since in the substrate solution, every reactive species is active and one electron is trapped, the photo-oxidation of NOR was improved by the additional DMSO. PBQ and IP are main scavenging agents for the NOR degradation in the presence of CA.

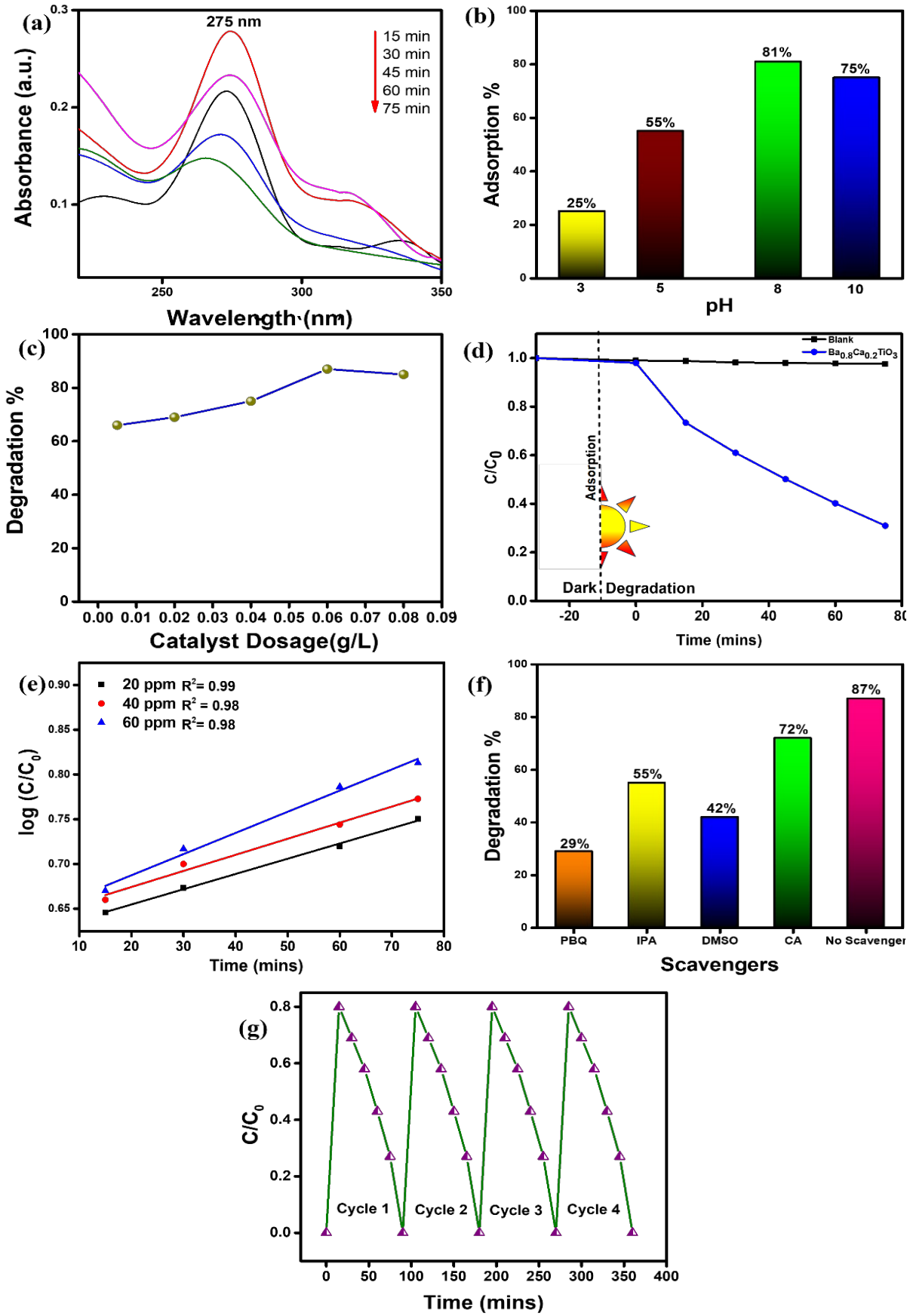

Figure 5. (a) Photodegradation of Norfloxacin (NOR) by $Ba_{0.8}Ca_{0.2}TiO_3$ at different time intervals, (b) Photodegradation of NOR by BCTO at different pH, (c) effect of catalyst dose, (d) rate of degradation of NOR at different time interval using the composite and blank, (e) Pseudo-first order kinetics at different concentration, (f) impact of several scavenging agents on the photodegradation process, and (g) Reusability of $Ba_{0.8}Ca_{0.2}TiO_3$.

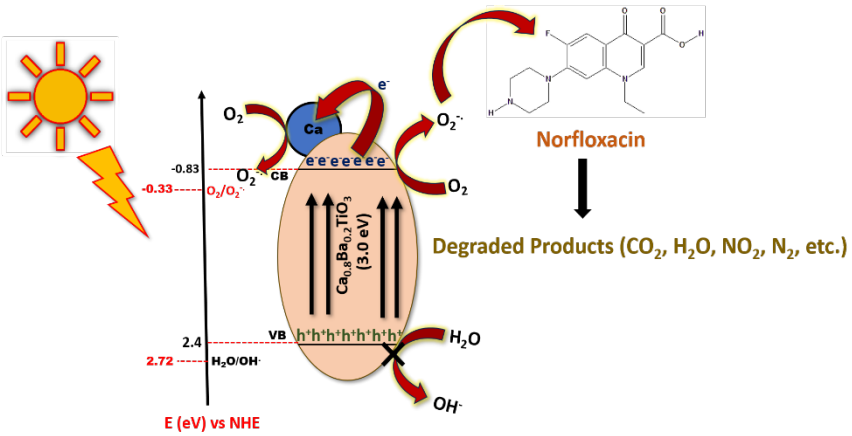

Figure 6. Mechanism for degradation of Norfloxacin

3.7.7 Plausible mechanism

By measuring the band edge potential of $Ba_{0.8}Ca_{0.2}TiO_3$, the mechanistic pathway leading to photocatalytic activity can be well defined. The following formula is used to calculate the E_{VB} and E_{CB} edge potentials:

$$E_{VB} = \chi - E_e + 0.5E_g \quad (9)$$

$$E_{CB} = E_{VB} - E_g \quad (10)$$

Where "χ" is referred to as the absolute electronegativity of $Ba_{0.8}TiO_3$ is 5.27 eV [36]. On the hydrogen scale, the free electrons energy (E_e) approaches 4.5 eV. According to the Kubeka Monk calculation, the E_g of $Ba_{0.8}Ca_{0.2}TiO_3$is 3.0 eV, while E_g of $Ba_{0.8}TiO_3$ is 3.2 eV. Using the aforementioned calculation, the valence band edge potential E_{VB} is 2.4 eV, whereas the conduction band edge potential E_{CB} is –0.83 eV. The E_{VB} is less positive than the redox potential of $^{\bullet}OH/H_2O$ which is 2.72 eV. This suggests that hydroxyl radical ($^{\bullet}OH$) generation is constrained. The study revealed that super oxide ($^{\bullet}O_2^-$) is the main radical responsible for the photocatalytic breakdown of Norfloxacin not ($^{\bullet}OH$).

Figure 6 depicts the photocatalytic degradation route according to band location. When light strikes the catalyst's surface, electrons are transferred between the VB and the CB. Therefore, holes are generated at the VB, but these holes are insufficient to oxidise H_2O/OH^- to $^{\bullet}OH$ as its VB is more negative than the potential of $H_2O/^{\bullet}OH$ (2.72 V vs NHE). As a result, the e^-s interacts with O_2 to generate $O_2^{-\cdot}$ radicals. The following is the most plausible mechanism for producing reactive oxidative radicals:

$$BCTO + h\nu \longrightarrow BCTO\left(h^+_{VB} + e^-_{CB}\right) \quad (11)$$

$$H^+ + H_2O \longrightarrow OH^- \quad (12)$$

$$O_2 + e^- \longrightarrow O_2^- \quad (13)$$

$$\cdot O_2^- + 2H^+ \longrightarrow 2HO_2 \quad (14)$$

$$2HO_2 \longrightarrow H_2O_2 + O_2 \quad (15)$$

$$\cdot O_2^- + \text{Norfloxacin } CO_2 + H_2O \quad (16)$$

4. Conclusion

The $Ba_{0.8}Ca_{0.2}TiO_3$ (BCTO) perovskite composite which was synthesised through a simple solid-state method which exhibits exceptional photocatalytic performance for the degradation of the pharmaceutical contaminant norfloxacin. The various characteristics of BCTO reveals its well-defined structural, optical and electrical properties, which adds up to the high efficiency in photocatalytic activity. The composite exhibits an extraordinary degradation rate of 87%, with the enhanced photocatalytic activity attributed to its enhanced charge carrier mobility, decreased electron-hole recombination and increased light harvestation. Kinetic studies confirms that the degradation follows a pseudo-first order reaction model, which indicates its potential for large-scale environmental applications. Additionally, BCTO surpasses pure $BaTiO_3$ and traditional photocatalysts, establishing it as a potential choice for treating persistent pharmaceutical contaminants in water and wastewater treatment. From the FE-SEM, EDS and elemental analysis the photocatalytic degradation of NOR was confirmed. All the findings strongly suggest that $Ba_{0.8}Ca_{0.2}TiO_3$ material is one of the most sustainable materials that would play a significant role in advancing sustainable environmental remediation technologies.

References

[1] A. Khanna N. Kumar, R. Rana, Jyoti, A. Sharma, Muskan, H. Kaur, and P. M. S. Bedi, "Fluoroquinolones tackling anti-microbial resistance: Rational design, mechanistic insights and comparative analysis of norfloxacin vs ciprofloxacin derivatives," *Bioorganic Chemistry*, vol. 153, p. 107773, 2024.

[2] R. Mithuna, R. Tharranyalakshmi, I. Jain, S.Singhal, D. Sikarwar, S. Das, J.Ranjitha, D. Ghosh, M. M. Rahman, and B. Das, "Emergence of antibiotic resistance due to the excessive use of antibiotics in medicines and feed additives: A global scenario with emphasis on the Indian perspective," *Emerging Contaminants*, vol. 10, no. 4, p. 100389, 2024.

[3] A. Subhadarshini, E. Subudhi, P. G. R. Achary, S. A. Behera, N. Parwin, and B. Nanda, "ZIF-8 supported Ag_3PO_4/g-C_3N_4 a double z-scheme heterojunction: An efficient photocatalytic,

antibacterial and hemolytic nanomaterial," *Journal of Water Process Engineering*, vol. 65, p. 105901, 2024.

[4] B. Nanda, S. A. Behera, A. Subhadarshini, P. M. Mishra, and P. G. R. Achary, "Sunlight assisted photocatalytic degradation of antibiotics by boron-doped lanthanum ferrite," *Journal of Molecular Structure*, vol. 1306, p. 137921, 2024.

[5] F. Li, S. Yue, Z. Zhao, K. Liu, P. Wang, and S. Zhan, "Application of molecularly imprinted polymers in the water environmental field: A review on the detection and efficient removal of emerging contaminants," *Materials Today Sustainability*, p. 100904, 2024.

[6] A. Mary Ealias, G. Meda, and K. Tanzil, "Recent progress in sustainable treatment technologies for the removal of emerging contaminants from wastewater: A review on occurrence, global status and impact on biota," *Reviews of Environmental Contamination and Toxicology*, vol. 262, no. 1, p. 16, 2024.

[7] S. A. Behera, A. Subhadarshini, S. S. Bhuyan, B. Nanda, and P. G. R. Achary, "PVDF/rGO/CuO nanocomposites: A robust platform for solar-driven tetracycline photodegradation," *Inorganic Chemistry Communications*, vol. 160, p. 111995, 2024.

[8] S. A. Behera, A. Amanat, and P. G. R. Achary, "Photocatalytic degradation of ciprofloxacin drug utilizing novel PVDF/ polyaniline/lanthanum strontium manganate@ Ag composites," *Journal of Metals Materials and Minerals*, vol. 34, no. 1, p. 1896, 2024.

[9] P. Norranattrakul, K. Siralertmukul, and R. Nuisin, "Fabrication of chitosan/titanium dioxide composites film for the photo-catalytic degradation of dye," *Journal of Metals Materials and Minerals*, vol. 23, no. 2, 2013.

[10] P. K. Sahu, A. Champati, A. Pradhan, and B. Naik, "Design and development of nanostructured photocatalysts for large-scale solar green hydrogen generation," *Sustainable Energy & Fuels*, vol. 8, no. 9, pp. 1872-1917, 2024.

[11] M. A. Zazouli, Z. Yousefi, E. Babanezhad, R. A. Mohammadpour, and A. Ala, "Evaluating the effectiveness of advanced oxidation processes for leachate treatment: A systematic review," *Environmental Health Engineering and Management Journal*, vol. 11, no. 1, pp. 105-125, 2024.

[12] M. T. Samadi, A. Rezaie, A. A. Ebrahimi, A. Hossein Panahi, K. Kargarian, and H. Abdipour, "The utility of ultraviolet beam in advanced oxidation-reduction processes: a review on the mechanism of processes and possible production free radicals," *Environmental Science and Pollution Research*, vol. 31, no. 5, pp. 6628-6648, 2024.

[13] P. K. Sahu, A. Champati, A. Pradhan, N. K. Sahoo, and B. Naik, "Monoclinic ZrO_2 nanospheres supported nitrogen-enriched carbon nitride nanosheets for efficient photodegradation of ciprofloxacin," *Journal of Nanoparticle Research*, vol. 26, no. 11, p. 261, 2024.

[14] A. Panda, K. K. Das, K. R. Kaja, M. Belal, and B. K. Panigrahi, "Single electrode mode triboelectric nanogenerator for recognition of animal sounds," *Journal of Metals Materials and Minerals*, vol. 34, no. 4, p. 2170, 2024.

[15] M. Abedi, H. Basheer, L. Lakatos, A. Kukovecz, Z. Konya, T. Gyulavari, and Z. Pap, "Influence of rapid heat treatment on the photocatalytic activity and stability of barium titanates against a broad range of pollutants," *Molecules*, vol. 29, no. 22, p. 5350, 2024.

[16] L. Meng, L. Zhou, C. Liu, H. Jia, Y. Lu, D. Ji, T. Liang, Y. Yuan, X. Zhang, Y. Zhu, Y. Jiang, P. Guan, Y. Zhou, Q. Zhang, T. Wan, M. Li, Z. Li, R. Joshi, Z. Han, and D. Chu, "Synergistic barium titanate/MXene composite as a high-performance piezo-photocatalyst for efficient dye degradation," *Journal of Colloid and Interface Science*, vol. 674, pp. 972-981, 2024.

[17] T. L. Vu, H. T. Nguyen, H. L. Nguyen, N. T. Nguyen, D. Q. Van, and D. D. Dang, "Theoretical studies on the magnetic, electrical, and optical properties of lead-free ferroelectric $Ba(Zr_{0.2}Ti_{0.8})O_3$ materials with manganese doping," *Dalat University Journal of Science*, pp. 95-112, 2024.

[18] N. H. Ngan, V. T. Larn, N. H. Lam, P. T. Huyen, T. H. Nguyen, D. D. Dung, and D. Q. Van, "Structural, electronic and optical properties of complex lead-free ferroelectric $Ba_{0.7}Ca_{0.3}TiO_3$ materials: A DFT study," *MRS Communications*, vol. 14, no. 4, pp. 667-675, 2024.

[19] Z. Hasan, M. A. Rahman, D. K. Das, and H. K. Rouf, "Influence of Ca doping in structural, electronic, optical and mechanical properties of $Ba_{1-x}Ca_xTiO_3$ perovskite from first-principles investigation," *Scientific Reports*, vol. 13, no. 1, p. 10487, 2023.

[20] A. Saidi, A. Mabrouki, R. Dhahri, E. Dhahri, K. Khirouni, and B. F. O. Costa, "Electronic, electrical and thermoelectric properties of $Ba_{0.95}Ca_{0.05}Ti_{0.95}Y_{0.05}O_2$. 975 compound: Experimental study and DFT-mBJ calculation," *Heliyon*, vol. 9, no. 8, 2023.

[21] H. J. Sumona, A. Al Mahmood, M. B. Islam, J. H. Kasem, and M. S. Rahman, "Modification of structural, morphological, and dielectric properties of barium calcium titanate ceramics with yttrium addition," *Heliyon*, vol. 10, no. 5, 2024.

[22] E. E. Yilmaz, E. B. Kocsma, H. E. Figen, and M. K. Elibol, "Physicochemical characterization of calcium-doped barium zirconate perovskites for hydrogen-induced systems and their life cycle assessment," *International Journal of Hydrogen Energy*, 2025.

[23] M. V. Paranjape, S. A. Graham, P. Manchi, A. Kurakula, and J. S. Yu, "Multistage $SrBaTiO_3$/PDMS composite film-based hybrid nanogenerator for efficient floor energy harvesting applications," *Small*, vol. 19, no. 27, p. 2300535, 2023.

[24] E. Cai, S. Peng, and Q. Liu, "Superior piezoelectricity in lead-free barium titanate piezoceramics," *Journal of Materials Science*, vol. 10, no. 3, pp. 694-706, 2024.

[25] A. Salhi, S. Sayouri, A. Alimoussa, and L. Kadira, "Impedance spectroscopy analysis of Ca doped $BaTiO_3$ ferroelectric ceramic manufactured with a new synthesis technique," *Materials Today: Proceedings*, vol. 13, pp. 1248-1258, 2019.

[26] J.-S. Park, Y.-H. Lee, K.-B. Kim, and Y.-I. Kim, "Structural study of Ca doped barium titanate," *Nuclear Instruments and Methods in Physics Research Section B: Beam Interactions with Materials and Atoms*, vol. 284, pp. 44-48, 2012.

[27] D. Sun, X. Jin, H. Liu, J. Zhu, Y. Zhu, and Y. Zhu, "Investigation on FTIR spectrum of barium titanate ceramics doped with alkali ions," *Ferroelectrics*, vol. 355, no. 1, pp. 145-148, 2007.

[28] A. Salhi, S. Sayouri, and M. Haddad, "Optical properties of calcium-doped barium titanate prepared by sol-gel route and

microwave pre-treatment," *Optical materials (Amsterdam. Online)*, vol. 133, p. 113008, 2022.

[29] S. A. Behera, D. Khatua, R. K. Singh, R. N. P. Choudhary, and P. G. R. Achary, "Temperature-Dependent electrical and dielectric characteristics of lead germanate $Pb_5Ge_{1.5}Sn_{1.5}O_{11}$," *Inorganic Chemistry Communications*, vol. 163, p. 112370, 2024.

[30] R. K. Mishra, A. Yadav, V. Mishra, S. N. Mishra, D. S. Singh, and D. K. Verma, "Fundamental theory of electromagnetic spectrum, dielectric and magnetic properties, molecular rotation, and the green chemistry of microwave heating equipment," *Green Chemical Synthesis with Microwaves Ultrasound*, pp. 21-67, 2024.

[31] S. A. Behera, R. N. P. Choudhary, and P. G. R. Achary, "Electrical and dielectric properties of EVA/modified lead titanate elastomer composites," *Materials Today: Proceedings*, 2023.

[32] D. Prajapati, V. S. Rai, B. Jena, H. Verma, A. Kumar, N. B. Singh, and K. D. Mandal, "Evolution of microstructure, dielectric, and electrical properties of Nd-doped BCTO synthesized via semi-wet route," *Journal of Nanoparticle Research*, vol. 26, no. 2, p. 30, 2024.

[33] T. Zhou, X. Huang, D. Zhang, W. Liu, and X. Li, "Design and simulation for minimizing non-radiative recombination losses in $CsGeI_2Br$ perovskite solar cells," *Nanomaterials*, vol. 14, no. 20, p. 1650, 2024.

[34] S. Kalingani, S. N. Das, and S. Bhuyan, "Dielectric and conductive properties of $ZnMoO_4$-TiO_2: Exploring high-temperature performance and application potential," *Brazilian Journal of Physics*, vol. 54, no. 6, pp. 1-13, 2024.

[35] S. A. Behera, S. Hajra, S. Panda, A. Amanat, and P. G. R. Achary, "Structural and electrical properties of $0.98(K_{0.5}Na_{0.5}NbO_3)$-$0.02(Bi_{0.5}Na_{0.5}TiO_3)$ ceramics," *Journal of Metals, Materials and Minerals*, vol. 33, no. 4, p. 1894, 2023.

[36] A. Sudhakaran, A. Sudhakaran, and E. Sivasenthil, "Electron density effect of hybrid ferrites on structural, spectroscopic, optical, and magnetic properties in $(BaTiO_3)(1-x)+(ZnFe_2O_4)$ x nanoceramics," *Journal of Materials Science: Materials in Electronics*, vol. 34, no. 2, p. 104, 2023.